

# Interfacial Reactions and Spacer-Dependent Ordering in FePt-C/X-C/FePt-C (X = Ir, Pt, Ag) Trilayer Nanostructures

*Daisuke Ogawa<sup>1</sup>, Yusuke Matsuoka<sup>1</sup>, Yuta Sasaki<sup>1</sup>, Anton Bolyachkin<sup>1</sup>, Shinji Isogami<sup>1</sup>, Machiko Ode<sup>1</sup>, Taichi Abe<sup>1</sup>, Shinya Kasai<sup>1</sup>, \*Yukiko K. Takahashi<sup>1,2</sup>*

<sup>1</sup>*National Institute for Materials Science, 1-2-1 Sengen, Tsukuba, Japan*

<sup>2</sup>*RIEC, Tohoku university, 2-1-1 Katahira, Sendai, Japan*

Corresponding author : Y.K. Takahashi, takahashi.yukiko@nims.go.jp

## ABSTRACT

Spacer layers critically influence nanoscale interfacial reactions, strain transfer, microstructural evolution in FePt-based multilayer films. Here, FePt-C/X-C/FePt-C trilayer systems (X = Ir, Pt, Ag) are employed to examine how spacer material governs thermodynamic stability and interfacial chemistry. Distinct spacer-dependent behaviors are identified. Ir promotes strong wetting which results in network-like FePt morphologies, Ag is immiscible with FePt which leads to granular isolation but loss of epitaxial continuity, and Pt undergoes interfacial interdiffusion which forms an L<sub>12</sub>-ordered reaction phase at the spacer position.

Detailed structural and compositional characterization shows that the Pt spacer forms an L<sub>12</sub>-FePt<sub>3</sub> interlayer with a sharp and thermodynamically stable interface against the adjacent L<sub>10</sub>-FePt layers. However, despite the formation of this ordered reaction phase and coherent epitaxial compatibility, the top FePt layer exhibits a reduced degree of L<sub>10</sub> ordering accompanied by a decrease in coercivity, indicating that the L<sub>12</sub> spacer does not provide sufficient strain-mediated driving force to enhance ordering in the overgrown FePt layer. This limitation arises from the small lattice misfit between the two ordered phases, which favors interface coherence but imposes only weak epitaxial strain.

Phase-field simulations based on CALPHAD thermodynamic data are employed to estimate the equilibrium upper bound of the  $L1_0/L1_2$  interfacial width, confirming that the reaction-formed spacer can remain structurally stable within nanometer-scale thicknesses. The present results demonstrate that thermodynamic stability and magnetic neutrality of spacer phases are necessary but not sufficient conditions for functional spacer design. In addition to interfacial stability, the ability of a spacer to impose sufficient epitaxial strain to enhance  $L1_0$  ordering in the top FePt layer emerges as a critical design requirement. These findings provide general guidelines for spacer design in ordered alloy multilayers, extending beyond the Fe-Pt system.

#### KEYWORDS

Ordered alloy, multilayers, Interfacial reactions, FePt, Phase-field simulation

## 1. INTRODUCTION

Vertically stacked magnetic-thin-film architectures have attracted increasing attention across a wide range of magnetic and spintronic technologies, although the motivations for vertical integration differ depending on the application. In magnetic recording and memory technologies, vertical stacking is explored as a strategy to overcome the scaling limitations of planar structures by increasing information density without further reduction of lateral feature sizes<sup>1-6</sup>. In contrast, in spintronic devices such as magnetic tunnel junctions, multilayer stacking is employed primarily to enable specific functionalities arising from interfacial spin-dependent transport<sup>7-12</sup>, magnetic anisotropy engineering<sup>12-14</sup>, and symmetry filtering<sup>15-17</sup>, rather than to increase device density. Despite these differing motivations, a common feature of vertically integrated magnetic structures is that the properties of each layer are strongly governed by interfacial reactions, strain transfer, and phase stability at the nanoscale.

Among the various magnetic materials employed in vertically stacked architectures, chemically ordered alloys provide a particularly stringent model system for examining interfacial effects. In such materials, magnetic anisotropy and thermal stability are directly linked to long-range chemical ordering<sup>18</sup>, making them highly sensitive to interfacial reactions and epitaxial constraints<sup>19</sup>. As a representative example, L1<sub>0</sub>-ordered FePt exhibits extremely large magnetocrystalline anisotropy originating from its chemically ordered structure<sup>20,21</sup>, and even modest perturbations to ordering or strain can lead to pronounced changes in magnetic properties<sup>22-26</sup>.

When FePt layers are vertically stacked, the preservation and regeneration of L1<sub>0</sub> ordering in each layer become decisive challenges. In contrast to planar or single-layer films, the growth of an upper FePt layer is strongly influenced by the underlying spacer, which mediates interfacial chemistry, strain transfer, and crystallographic registry. Consequently, spacer layers in FePt-based multilayers are not passive separators but active elements that determine whether high L1<sub>0</sub> ordering and magnetic hardness can be achieved in the overgrown layer. This sensitivity makes FePt an ideal model system for revealing materials-level constraints that may remain obscured in magnetically softer or structurally more tolerant systems.

In FePt-based three-dimensional magnetic architectures, vertical stacking is considered in the context of multilayer devices such as magnetic tunnel junctions (MTJs) employing perpendicularly magnetized FePt electrodes<sup>27-29</sup> and three-dimensional heat-assisted magnetic recording (3D-

HAMR) media<sup>2,30</sup>. In these systems, spacer layers are introduced to magnetically separate adjacent FePt layers while maintaining crystallographic coherence. Unlike magnetically soft multilayers, however, FePt-based structures are highly sensitive to chemical ordering, and even subtle perturbations at the interface can lead to pronounced changes in magnetic anisotropy.

From a materials perspective, spacer layers in vertically stacked FePt structures inevitably participate in interfacial reactions during high-temperature processing. Indeed, in 3D-HAMR configurations employing Ru spacers, interdiffusion of Ru has been reported to reduce the degree of L1<sub>0</sub> ordering in FePt layers grown above the spacer<sup>2,30</sup>, highlighting that spacer diffusion can directly degrade ordering in vertically integrated FePt structures. More recently, complementary interface engineering strategies have been explored in magnetic multilayers, including FePt-based systems<sup>19,24,26</sup>, to control interdiffusion, strain coupling, and chemical ordering. These studies demonstrate that nanoscale interface structure critically governs magnetic anisotropy and structural evolution in vertically integrated systems<sup>31</sup>. Although such interface-driven approaches are increasingly recognized, experimental demonstrations in FePt-based three-dimensional architectures remain limited, particularly in the context of 3D-HAMR media. Consequently, a systematic materials-level understanding of how spacer chemistry, miscibility, and lattice compatibility collectively influence L1<sub>0</sub> ordering across multilayer interfaces is still lacking. More generally, interdiffusion, phase formation, and strain accommodation at the FePt/spacer interface cannot be assumed a priori to be benign. While an ideal spacer would suppress magnetic coupling without compromising chemical ordering, whether such a requirement can be satisfied without inhibiting ordering and anisotropy in the overgrown FePt layer remains a nontrivial materials question.

In this study, we systematically examine spacer design in FePt–C/X–C/FePt–C trilayer structures using X = Ir, Pt, and Ag, which represent three distinct classes of spacer behavior: wetting-dominated, reaction-forming, and immiscible systems. We employ detailed microstructural and compositional analyses to directly elucidate interfacial reactions, diffusion behavior, and phase formation during high-temperature deposition.

From a crystallographic perspective, the lattice compatibility between spacer layers and L1<sub>0</sub>-FePt varies among the metallic spacers examined in this study. Ir exhibits a very small lattice misfit of -0.3% relative to L1<sub>0</sub>-FePt, whereas Pt and Ag show positive but still moderate misfits of 2.1%

and 6.2%, respectively. These misfit values are smaller than those typically encountered for oxide substrates such as MgO, ~9 %. Emphasis is placed on correlating spacer-dependent interfacial structures with the resulting degree of  $L1_0$  ordering and magnetic response of the overgrown FePt layer. Through this comparative approach, we identify suitable materials and design guidelines for spacer layers in ordered-alloy multilayers relevant to three-dimensional magnetic architectures.

## 2. Methodology

### 2.1 Thin-film preparation and structural characterization

All the films were prepared using an ultrahigh-vacuum co-sputtering system with a base pressure of  $\sim 10^{-7}$  Pa. A multilayer with the film stack of FePt-C(4.5 nm)/X-C(2.9~3.0 nm)/FePt-C(4.5 nm) was grown at 500 °C on MgO(001) single crystal substrate. X is the spacer layer material, i.e. Ir, Pt and Ag. A carbon capping layer was deposited at room temperature to prevent the surface damage. The deposition temperature of 500 °C was selected to ensure sufficient development of  $L1_0$  ordering during growth, consistent with established processing conditions for FePt-based granular films<sup>2</sup>.

X-ray diffraction (XRD) Rigaku SmartLab with a Cu X-ray source was used for estimation of crystallographic and degree of  $L1_0$  order. Electron-transparent thin specimens for a cross-sectional microstructure analysis were prepared for transmission electron microscopy (TEM) using a focused ion beam lift-out technique (FEI Helios Nanolab 650). To prevent damage during the ion beam milling, the film surfaces were coated with Ni. TEM samples for in-plane observation were prepared by a chemical etching method. The etching solution was the mixture of phosphoric 98 vol % and sulfuric 2 vol % acids and etching was carried out at 150 °C. TEM was performed using a Titan G2 80-200 and Spectra Ultra (Thermo Fisher Scientific) with a probe aberration corrector.

A 7 T Quantum Design superconducting quantum interference device magnetometer (SQUID) was used for magnetic measurements. The films were embedded in high-temperature cement for the measurement at temperature above 380 K. The Curie temperature ( $T_c$ ) was determined by the least squares fitting of the temperature dependence of magnetization curve using Kuz'min's equation<sup>32</sup>;

$$M_s(T) = M_s(0) \left[ 1 - s \left( \frac{T}{T_c} \right)^{\frac{3}{2}} - (1 - s) \frac{T^{\frac{5}{2}}}{T_c^{\frac{5}{2}}} \right]^{\frac{1}{3}}, \quad (1)$$

Where,  $S = 0.176 \frac{g\mu_B}{M_s(0)} \left( \frac{k_B T_c}{D} \right)^{\frac{3}{2}}$ ,  $g$  is Landé g-factor,  $\mu_B$  is Bohr magneton,  $k_B$  is Boltzmann constant and  $D$  is a spin wave stiffness which is valid in the limit  $q \rightarrow \infty$ , where  $q$  is wave vector.

Magneto-optical Kerr effect (MOKE) from front and back side was performed using a femtosecond laser source with a duration, pulse width, and center wave length of 10 kHz, 290 fs, and 1028 nm, respectively. A superconductive magnet chamber, a Quantum Design Opticool system, was used for the MOKE measurement.

## 2.2 Phase-field simulation of the L1<sub>0</sub>/ L1<sub>2</sub> interface

While sputter deposition is inherently a non-equilibrium process, the high deposition temperature (500 °C) facilitates atomic diffusion, allowing the interface structure to evolve towards a local thermodynamic equilibrium state. To evaluate the equilibrium interface thickness of the L1<sub>0</sub>-FePt-L1<sub>2</sub>-FePt<sub>3</sub> interface, phase-field (PF) simulations<sup>33</sup> are performed to calculate the equilibrium Pt concentration profile across the L1<sub>0</sub>-FePt-L1<sub>2</sub>-FePt<sub>3</sub> interface. The order parameter employed is the local Pt concentration ( $c$ ), and the time evolution of the concentration field is calculated by solving the Cahn-Hilliard equation<sup>34</sup>.

$$\frac{\partial c}{\partial t} = \frac{\partial}{\partial x} \left( M \frac{\partial}{\partial x} \frac{\delta G_{\text{sys}}}{\delta c} \right) \quad (2)$$

Here,  $t$  is time,  $x$  is spatial coordinates,  $M$  is the diffusion mobility, and  $G_{\text{sys}}$  is the Gibbs energy of the system. The Gibbs energy of the system ( $G_{\text{sys}}$ ) is expressed as the sum of the chemical Gibbs energy ( $G_{\text{chem}}$ ) and the gradient energy ( $G_{\text{grad}}$ ).

$$G_{\text{sys}} = G_{\text{chem}} + G_{\text{grad}} \quad (3)$$

$$= G_{\text{chem}} + \kappa \left( \frac{\partial c}{\partial x} \right)^2 \quad (4)$$

where  $\kappa$  is the gradient energy coefficient, which describes the excess energy due to the concentration gradient. For the chemical Gibbs energy ( $G_{\text{chem}}$ ), the Gibbs energies calculated in the range of 49~76 at.% using the CALPHAD database recently developed by Tanaka *et al.*<sup>35</sup> were fitted to a 10th-order equation and used in the simulation.

As the objective of this calculation is to obtain the equilibrium profile, composition profiles are obtained after sufficient time has elapsed at 500 °C. Consequently, the results are independent of the diffusion mobility. The interface width is measured by determining the region where the Pt concentration deviates by 0.5 at.% or more from the equilibrium compositions of FePt and FePt<sub>3</sub>, based on the resulting equilibrium concentration profiles.

### 3. RESULTS

#### 3.1 Ir spacer: wetting-dominated interfacial morphology

Fig. 1(a) shows a bright-field (BF) in-plane transmission electron microscopy (TEM) image of the FePt-20vol.%C(4.5 nm)/Ir-20vol.%C(2.9 nm)/FePt-20vol.%C(4.5 nm) trilayer film. The film exhibits a network-like microstructure, attributed to the high wettability of Ir spacer on the bottom FePt. The selected area electron diffraction (SAED) pattern shown in Fig. 1(b) reveals a zone axis of [001], indicating that the FePt grains are highly textured along the (001) direction. The presence of (110) superlattice reflections confirms L1<sub>0</sub> ordering. A cross-sectional high-angle annular dark-field scanning TEM (HAADF-STEM) image shown in Fig. 1(c) illustrates that the bottom FePt layer consists of laterally separated crystallographic grains with an average in-plane size of ~15 nm (measured parallel to the substrate surface). In contrast, the top FePt layer exhibits partial lateral coalescence of FePt grains, resulting in a network-like morphology rather than fully isolated grains. A schematic illustration of this lateral coalescence in the Ir-spacer sample is provided in the Graphical Abstract for clarity. This interconnected nature is more clearly observed in the

elemental mapping images obtained via energy-dispersive X-ray spectroscopy (EDS), as displayed in Fig. 2(a)–2(e). The formation of this network-like morphology is likely a consequence of favorable wetting behavior arising from low effective interfacial energy between FePt and Ir. While the surface free energies of FePt(001) and Ir(001) are reported to be 2.1 J/m<sup>2</sup><sup>36</sup> and 2.7–3.0 J/m<sup>2</sup><sup>37,38</sup>, respectively, these comparable values suggest that surface energy alone cannot account for the observed wetting behavior. Instead, the experimentally observed morphology indicates favorable interfacial energetics at the FePt/Ir interface, which promotes extensive wetting and the development of network-like FePt structures. The X-ray diffraction (XRD) pattern of the trilayer film shown in Fig. 1(d) reveals clear (001) and (002) peaks from FePt at  $2\theta = 23.8^\circ$  and  $47.9^\circ$ , respectively, along with a weak Ir (002) peak near  $47^\circ$ . The degree of ordering ( $S$ ) for the L1<sub>0</sub> phase, calculated from the integrated intensity ratio of (001) and (002) peaks, was found to be 0.68. This value is slightly reduced compared to that of the single-layer FePt-20vol.% C film ( $S = 0.73$ <sup>2</sup>).

Magnetization curves of the film in the out-of-plane and in-plane directions are shown by red and blue lines, respectively, in Fig. 1(e). The easy axis of magnetization is perpendicular to the film plane, consistent with the observed crystallographic texture. The out-of-plane magnetization curve displays a two-step reversal process, with coercive fields ( $\mu_0 H_c$ ) of 0.4 T and 4.0 T, respectively. These distinct  $\mu_0 H_c$  likely correspond to the sequential switching of the top and bottom FePt layers. To further examine the layer-resolved switching behavior, front- and back-side magneto-optical Kerr effect (MOKE) measurements (Fig. 3(a)) were performed. By reversing the illumination direction, the relative magnetic contributions from the top and bottom FePt layers can be selectively enhanced. As shown in Fig. 3(b), the relative prominence of the low- and high-coercivity switching components changes depending on the illumination geometry, with back-side illumination enhancing the high-coercivity contribution. This observation indicates that the bottom FePt layer possesses higher coercivity and supports reduced interlayer exchange coupling and largely independent switching of the two FePt layers. The low  $\mu_0 H_c$  of 0.4 T, corresponding to the top FePt layer, is attributed to the absence of pinning sites for magnetic domain wall motion in the network-like morphology<sup>39,40</sup>. The inset of Fig. 1(e) shows the temperature dependence of magnetization. It shows a single  $T_c$  around 642 K. Fig. 2(g) shows the line profile of the composition of the rectangular area shown in Fig. 2(f). Because the bottom FePt has a round shape,



the degree of diffusion near the interface cannot be discussed, but Ir has diffused by around 10% in areas far from the interface. The bottom FePt shows high  $\mu_0 H_c$  of 4 T even 10at% Ir is mixed. The high  $\mu_0 H_c$  of FePt-Ir could be due to the enhancement of the perpendicular anisotropy originated from strong spin-orbit interaction of Ir<sup>41</sup>.

### 3.2 Pt spacer: reaction-formed L1<sub>2</sub> interlayer and ordering limitation

Fig. 4(a) displays the in-plane BF-TEM image of the FePt-20vol.%C(4.5nm)/Pt-20vol.%C(3nm)/FePt-20vol.%C(4.5nm) film. The microstructure reveals laterally separated, granular FePt grains with an average in-plane grain size of approximately 18.5 nm. In contrast to the Ir-spacer sample, both the top and bottom FePt layers exhibit clearly separated grains without lateral coalescence, as evidenced by distinct grain boundaries shown by arrows. The SAED pattern shown in Fig. 4(b) taken along the [001] zone axis confirms a strong (001) texture in most FePt grains. Additional weak diffraction spots, indicated by arrows, are attributed to L1<sub>2</sub>-FePt<sub>3</sub> ordering and/or in-plane variants of L1<sub>0</sub>-FePt. The in-plane variant means that the *c*-axis is oriented in the in-plane direction. The cross-sectional HAADF-STEM image shown in Fig. 4(c) further highlights the granular nature and good separation in the FePt grains. A high-resolution HAADF-STEM image shown in Fig. 4(d) shows that the bottom FePt layer exhibits strong L1<sub>0</sub> ordering with (001) texture, whereas the top layer also retains L1<sub>0</sub> ordering but displays in-plane variants, particularly at the edge region. Although pure Pt was deposited as the spacer, an L1<sub>2</sub>-ordered FePt<sub>3</sub> phase was observed. Elemental mapping via EDS (Fig. 5a–5d) indicates the presence of a Pt-rich spacer layer. Compositional analysis (Fig. 5e and 5f) reveals L1<sub>2</sub> phase has the composition of Fe<sub>23.8</sub>Pt<sub>76.2</sub>, consistent with the latest FePt phase diagram as shown in Fig. S1. Note that the L1<sub>2</sub>-FePt<sub>3</sub> phase is known to be an antiferromagnet with a Néel temperature of about 160 K<sup>42</sup>. The X-ray diffraction (XRD) pattern in Fig. 4(e) confirms this, showing peaks corresponding to both L1<sub>0</sub>-FePt and L1<sub>2</sub>-FePt<sub>3</sub> phases. In particular, the (002) reflections in the Pt-spacer sample exhibit multiple overlapping components. To clarify the phase contributions, peak fitting analysis was performed in the (002) diffraction region as shown in Fig. S2. The fitting reveals three components corresponding to the L1<sub>2</sub> spacer phase and two L1<sub>0</sub>-FePt components originating from the top and bottom FePt layers. In contrast, the (001) reflections of L1<sub>0</sub> and L1<sub>2</sub> strongly overlap in the present

XRD pattern, making reliable peak decomposition difficult. Therefore, the degree of  $L1_0$  order ( $S$ ) could not be quantitatively estimated from the XRD data for this sample.

The out-of-plane and in-plane magnetization curves shown in Fig. 4(f) exhibits strong perpendicular anisotropy, with a two-step magnetization reversal process with the  $\mu_0 H_c$  of 0.3 T and 2.5 T. The presence of distinct switching fields suggests reduced interlayer exchange coupling, attributed to the compositional and structural differentiation enabled by the  $L1_2$ -FePt<sub>3</sub> spacer.

As shown in Fig. 5(e) and (f), due to the diffusion of Fe and Pt, the compositions of the top and bottom FePt layers are Fe<sub>47.0</sub>Pt<sub>53.0</sub> and Fe<sub>46.4</sub>Pt<sub>53.6</sub>, respectively. As a result of the atomic diffusion, the composition of FePt layer changes to Pt-rich. This deviation from equiatomic composition is thought to be the cause of the decrease in anisotropy as well as in  $\mu_0 H_c$ . However, the difference in coercivity between the top and bottom FePt layers cannot be explained solely by the small compositional difference  $\sim 0.6$  at%. As discussed in S2, micromagnetic fitting of the demagnetization curves shown in Fig. S3 indicates a significantly lower magnetic anisotropy in the top FePt layer, corresponding to a reduced degree of  $L1_0$  ordering  $S < 0.5$ . The lower coercivity of the top layer is therefore primarily attributed to its reduced  $L1_0$  ordering rather than to the slight compositional variation between the two layers.

The temperature dependence of magnetization is shown in the inset of Fig. 4(f) further supports this interpretation. The kink around 400 K and the two Curie temperatures obtained from Kuz'min's fitting<sup>32</sup> (400 K and 580 K) are consistent with the coexistence of highly ordered and weakly ordered FePt layers. The higher  $T_c$  (580 K) is attributed to the bottom FePt layer with higher  $L1_0$  ordering, whereas the lower  $T_c$  (400 K) corresponds to the top layer with reduced ordering and magnetic anisotropy. This dual- $T_c$  behavior provides independent magnetic evidence of ordering differentiation across the Pt spacer.

### 3.3 Ag spacer: immiscibility-driven loss of epitaxial continuity

The FePt-20vol.%C(4.5 nm)/Ag-20vol.%C(3 nm)/FePt-20vol.%C(4.5 nm) trilayer film exhibited significant differences in microstructure compared to the Ir and Pt spacer systems. As shown in the bright-field TEM image in Fig. 6(a), both the top and bottom FePt layers are granular

and well-isolated. Cross-sectional HAADF-STEM image shown in Fig. 6(b) reveals that the top FePt grains do not grow on the bottom FePt grains. EDS mappings in Fig. 6(e)–6(h) show that the Ag is rejected from FePt grains. This indicates that Ag exhibits limited solubility under the deposition conditions used. The XRD pattern shown in Fig. 6(c) displays well-resolved (001) and (002) peaks for FePt, while no distinct Ag-related peaks are detected. The ordering parameter ( $S$ ) is 0.75, which is higher than those of the Ir and Pt samples. Out-of-plane magnetization curve in Fig. 6(d) shows the single magnetization reversal and high  $\mu_0 H_c$  of 3.5 T. This disruption of grain-on-grain growth implies that immiscible spacers can preserve ordering within individual layers while preventing crystallographic continuity required for vertically integrated architectures.

The pronounced rejection behavior observed only in the Ag-spacer system is consistent with the intrinsic immiscibility of the FePt-Ag system<sup>43</sup>. Notably, carbon is present in all FePt-C/X-C/FePt-C trilayers and is observed to segregate preferentially at grain boundaries as part of the granular FePt-C architecture, as shown in Fig. S3. However, this grain-boundary carbon segregation is common to all spacer systems investigated (Ir, Pt, and Ag), and no additional carbon enrichment uniquely associated with the Ag spacer interface was detected. These observations indicate that while carbon contributes to the overall granular morphology, the selective rejection behavior in the Ag case is primarily governed by intrinsic FePt-Ag immiscibility rather than carbon segregation effects.

## 4. DISCUSSION

### 4.1 Spacer-dependent interfacial reactions, microstructural evolution, and magnetic implications

The present results demonstrate that the microstructural evolution of FePt-based trilayer films is governed primarily by the interfacial reaction pathway imposed by the spacer material. These interfacial processes not only determine morphological and crystallographic characteristics but also directly influence the resulting magnetic behavior of the trilayer stacks. Although Ir, Pt, and Ag spacers have comparable thicknesses and were deposited under identical conditions, they exhibit qualitatively different interfacial behaviors that directly influence the morphology and crystallographic continuity of the FePt layers.

Ir spacers promote extensive wetting on the bottom FePt layer due to favorable FePt/Ir interfacial energetics, resulting in lateral spreading during overgrowth and the development of network-like morphologies in the top FePt layer. In contrast, Ag spacers are immiscible with FePt under the present deposition conditions, causing Ag segregation and suppression of epitaxial registry between the bottom and top FePt layers. While this immiscibility favors granular isolation, it simultaneously disrupts crystallographic continuity across the trilayer stack.

Pt spacers exhibit a distinct behavior characterized by interfacial interdiffusion and the formation of the  $L1_2$ -ordered FePt<sub>3</sub> reaction phase. This reaction phase is consistent with the FePt equilibrium phase diagram<sup>35</sup> and represents a thermodynamically stabilized interface between the two  $L1_0$ -FePt layers. Importantly, the formation of this ordered reaction layer suppresses extensive wetting and preserves a crystallographically well-defined  $L1_0$ -FePt/ $L1_2$ -FePt<sub>3</sub> interface, where the  $L1_0$  periodicity transitions clearly into the  $L1_2$  periodicity, as observed in the atomic-resolution elemental mapping shown in Fig. 5(e). This distinguishes the Pt spacer system from the Ir-based system, which exhibits lateral coalescence of the top FePt layer, and from the Ag-based system, where spacer rejection prevents vertical crystallographic continuity.

Peak fitting of the (002) XRD region shown in Fig. S4 further provides insight into the structural differentiation between the two FePt layers in the Pt-spacer system. The fitted components reveal contributions from the  $L1_2$ -FePt<sub>3</sub> spacer phase as well as two  $L1_0$ -FePt components originating from the top and bottom FePt layers. By combining this analysis with the layer-resolved MOKE measurements described in Fig. S5, which shows that the bottom FePt layer exhibits a higher coercivity than the top layer, the higher-angle peak near  $\sim 49.0^\circ$  can be attributed to the bottom FePt layer while the lower-angle peak near  $\sim 48.4^\circ$  corresponds to the top FePt layer. This assignment is also consistent with the well-established relationship that the  $c$ -axis lattice parameter of  $L1_0$ -FePt decreases with increasing degree of chemical ordering<sup>44</sup>.

These distinct interfacial behaviors are directly reflected in the magnetic responses of the trilayer films. In the Ir-spacer system, the bottom FePt layer exhibits enhanced coercivity, which may be associated with interfacial effects involving Ir and its strong spin–orbit interaction [41]. However, the network-like morphology of the top FePt layer reduces lateral isolation and leads to lower coercivity in that layer. In the Ag-spacer system, the immiscibility preserves high ordering within individual FePt layers, resulting in a high coercivity and single-step magnetization reversal.

Nevertheless, the loss of vertical crystallographic registry limits its applicability in vertically integrated multilayer architectures. In contrast, the Pt-spacer system exhibits two-step magnetization reversal, reflecting structurally differentiated top and bottom FePt layers. This reaction-stabilized interlayer provides structural differentiation between the two FePt layers, which manifests as distinct switching behavior and ordering asymmetry. However, interdiffusion-induced compositional deviation toward Pt-rich FePt reduces magnetic anisotropy in the top layer. Taken together, the magnetic behavior of each trilayer directly mirrors the underlying interfacial reaction pathway and microstructural evolution.

To generalize these observations, the spacer-dependent interfacial and microstructural evolution — together with the resulting magnetic behavior — can be understood in terms of three governing factors: (i) interfacial energetics controlling wetting behavior, (ii) chemical miscibility and phase stability dictating interfacial reactions, and (iii) crystallographic compatibility enabling or suppressing vertical epitaxial continuity.

The Ir, Ag, and Pt spacer systems represent three limiting cases within this framework: a wetting-dominated regime, an immiscible regime, and a reaction-stabilized regime. These regimes illustrate that spacer selection inherently involves trade-offs between lateral isolation, vertical crystallographic coherence, and magnetic functionality.

Rather than identifying a universally optimal spacer, the present results highlight that the suitability of a given spacer depends on which of these governing factors is prioritized for the targeted multilayer architecture.

## 4.2 Interface reaction in L1<sub>0</sub>/L1<sub>2</sub>

When L1<sub>0</sub>-FePt and L1<sub>2</sub>-FePt<sub>3</sub> are in equilibrium composition, no further diffusion should occur because they are already in an energetically stable composition. However, as theoretically demonstrated by Cahn *et al.*<sup>45</sup>, interfaces between two adjacent phases exhibit a finite width with a continuous composition change. Consequently, the interface between L1<sub>0</sub>-FePt and L1<sub>2</sub>-FePt is also expected to possess a finite, thermodynamically stable width (see the inset of Fig. 7), like observations in other materials<sup>46-48</sup>. For effective magnetic separation of the top and bottom FePt

layers, this interfacial width (i.e., the thickness over which the L1<sub>0</sub>-FePt composition changes to L1<sub>2</sub>-FePt<sub>3</sub>) must be sufficiently small compared with the total thickness of the spacer region. If the transition region becomes too thick, the two interfacial zones on either side of the spacer can merge, eliminating a distinct L1<sub>2</sub>-FePt<sub>3</sub> layer and preventing the magnetic separation.

This study employs a phase-field (PF) model to evaluate the L1<sub>0</sub>-FePt–L1<sub>2</sub>-FePt<sub>3</sub> interface width. The Gibbs energy used in the PF simulation is taken from the CALPHAD database recently developed by Tanaka *et al.*<sup>35</sup> Fig. 7 shows the calculated equilibrium Pt concentration profiles across the L1<sub>0</sub>-FePt and L1<sub>2</sub>-FePt<sub>3</sub> interfaces at 500°C. 500°C is the deposition temperature of the samples prepared here. Since specific gradient energy coefficients ( $\kappa$ ) for the L1<sub>0</sub>/L1<sub>2</sub> FePt interface are not well-established,  $\kappa = 1 \times 10^{-15}$ ,  $5 \times 10^{-15}$ , and  $1 \times 10^{-14}$  Jm<sup>2</sup>/mol were selected from a representative range commonly used in PF analyses to estimate the plausible equilibrium interface width ( $10^{-16} < \kappa < 10^{-14}$  Jm<sup>2</sup>/mol<sup>49-51</sup> as representative values). Consequently, the calculated widths should be regarded as an estimated range, acknowledging that a precise determination specific to the FePt system requires further investigation. The interface width was calculated to be 0.76, 1.72, and 2.44 nm for  $\kappa = 1 \times 10^{-15}$ ,  $5 \times 10^{-15}$ , and  $1 \times 10^{-14}$  Jm<sup>2</sup>/mol, respectively.

For a spacer thickness of ~4 nm (adjusted for the FePt<sub>3</sub> composition), the remaining pure L1<sub>2</sub> core width is calculated to be 1.56–3.24 nm. Although a pure core theoretically remains, indicating thermodynamic stability, the calculated widths are comparable to the spacer thickness, particularly for higher  $\kappa$  values, suggesting the current thickness approaches the lower stability limit. Additionally, the apparent interface width observed in TEM cross-sections may be exaggerated by the three-dimensional curvature of the interfaces.

### 4.3 Ordering limitation of the top FePt layer on L1<sub>2</sub> spacers

Despite the successful formation of an ordered and thermodynamically stable L1<sub>2</sub> reaction phase, the top FePt layer grown on the Pt spacer exhibits a reduced degree of L1<sub>0</sub> ordering and low coercivity. The lattice misfit between L1<sub>0</sub>-FePt and L1<sub>2</sub>-FePt<sub>3</sub> or Pt is relatively small, 0.3 % and 2.1 % respectively, resulting in limited in-plane strain imposed on the overgrown FePt layer.

Although small lattice mismatch is generally advantageous for maintaining epitaxial growth, epitaxial compatibility alone does not necessarily enhance chemical ordering in the overgrown layer. Previous studies have shown that sufficient epitaxial strain is required to enhance the driving force for  $L1_0$  ordering, particularly to suppress in-plane variants and promote strong (001) texture<sup>26</sup>. In strain-assisted ordering mechanisms, elastic distortion imposed by the underlayer layer contributes to stabilizing the tetragonal  $L1_0$  structure. In the present Pt spacer system, the small misfit between the two phases allows crystallographic registry but provides only weak elastic driving force, thereby significantly weakening this strain-mediated ordering mechanism.

#### **4.4 Thermodynamic stability versus functional spacer performance**

While Section 4.3 discussed strain-mediated ordering limitation, here we generalize the implications from a spacer design perspective. Phase-field simulations based on CALPHAD thermodynamic data provide further insight into the nature of the  $L1_0$ – $L1_2$  interface formed in the Pt spacer system. The calculated equilibrium concentration profiles indicate that the interface between  $L1_0$ -FePt and  $L1_2$ -FePt<sub>3</sub> remains thermodynamically stable with a finite width on the order of a few nanometers, even at elevated temperatures corresponding to the deposition conditions. These results establish an upper bound for the equilibrium interfacial width and confirm that the experimentally observed  $L1_2$  spacer can be stabilized within nanometer-scale thicknesses.

However, thermodynamic stability alone does not guarantee functional spacer performance with respect to promoting chemical ordering in adjacent FePt layers. While the reaction-formed  $L1_2$  spacer effectively suppresses uncontrolled interdiffusion and maintains a chemically well-defined interface, it does not provide the epitaxial driving force required to enhance  $L1_0$  ordering in the overgrown FePt layer.

From a spacer design perspective, the present results demonstrate that reaction-formed ordered phases such as  $L1_2$ -FePt<sub>3</sub> can satisfy the requirements of thermodynamic compatibility and magnetic neutrality, yet may be intrinsically limited in their ability to act as ordering templates. While a precise numerical threshold for the required epitaxial strain is difficult to define universally due to process dependencies, our findings suggest a critical trade-off: a positive lattice misfit is necessary to induce tensile strain for  $L1_0$  ordering, yet excessive misfit risks interfacial

instability similar to the Ag spacer system. Thus, optimal spacer selection must balance sufficient positive misfit to drive ordering with stability constraints to prevent rejection. Achieving both interfacial stability and enhanced ordering therefore requires spacer materials or architectures that combine thermodynamic stability with more effective strain transfer or crystallographic constraint across the interface.

## 5. CONCLUSION

In this study, spacer design principles in FePt-C/X-C/FePt-C trilayer alloys ( $X = \text{Ir, Pt, Ag}$ ) were systematically investigated from the viewpoint of interfacial reaction, thermodynamic stability, and their impact on microstructural evolution. Rather than demonstrating device-level magnetic performance, the present work aimed to clarify the materials constraints that govern spacer functionality in ordered alloy multilayers.

Distinct spacer-dependent behaviors were identified. Ir spacers exhibited strong wetting on the bottom FePt layer, leading to network-like morphologies and interconnection of the top FePt grains. Ag spacers were immiscible with FePt, resulting in well-isolated granular microstructures but loss of epitaxial continuity between the bottom and top FePt layers. In contrast, Pt spacers underwent interfacial interdiffusion and stabilized an  $L_{12}$ -ordered FePt<sub>3</sub> reaction phase at the spacer position, forming a structurally sharp and thermodynamically stable interface with adjacent  $L_{10}$ -FePt layers.

Despite the successful formation of the  $L_{12}$  reaction phase, the top FePt layer grown on the  $L_{12}$  spacer exhibited a reduced degree of  $L_{10}$  ordering and low coercivity. This result indicates that thermodynamic stabilization of an ordered spacer phase alone does not guarantee favorable growth conditions for highly ordered  $L_{10}$ -FePt. The limited enhancement of ordering is attributed to insufficient lattice strain across the  $L_{12}$ - $L_{10}$  interface, arising from the small lattice misfit between the two ordered phases.

Phase-field simulations based on CALPHAD thermodynamic data provided an estimate of the equilibrium upper bound of the  $L_{10}$ - $L_{12}$  interfacial width, confirming that reaction-formed  $L_{12}$



spacers can remain structurally stable within nanometer-scale thicknesses. These simulations serve as a thermodynamic reference rather than a kinetic description of the deposition process.

Based on these findings, functional spacer design in FePt-based multilayer films requires satisfaction of the following four conditions:

- (i) thermodynamic stability of the spacer phase against adjacent magnetic layers,
- (ii) controlled interfacial reactions that avoid excessive intermixing,
- (iii) magnetic inertness of the spacer, and
- (iv) the ability to impose sufficient epitaxial strain to promote  $L1_0$  ordering in the overgrown FePt layer.

The present results demonstrate that  $L1_2$ -FePt<sub>3</sub> spacers fulfill the first three criteria but fail to meet the fourth, highlighting a fundamental limitation of reaction-formed  $L1_2$  spacers for promoting high ordering in the top FePt layer. While the detailed interfacial reaction pathway was most extensively analyzed for the Pt spacer, the four criteria also provide a useful framework for evaluating the Ir and Ag spacer systems. The Ir spacer satisfies conditions (i)–(iii). Its favorable wetting behavior preserves vertical epitaxial continuity and promotes lateral spreading of the top FePt layer. The resulting grain coalescence increases the effective FePt volume, which may thermodynamically favor  $L1_0$  ordering. However, this same wetting tendency compromises granular isolation and limits lateral scalability. The Ag spacer fulfills conditions (ii) and (iii) through immiscibility and magnetic inertness; however, its lack of crystallographic compatibility compromises vertical epitaxial continuity, limiting its applicability in structurally coherent multilayer architectures.

Looking forward, promising spacer candidates include refractory metals (e.g., Mo) and oxide-based materials such as MgO or MgTiO, which may offer improved diffusion resistance and enhanced lattice constraint. However, in FePt-C granular films, carbon segregation at FePt surfaces and surface-energy mismatch between metallic FePt and ionic oxides may hinder coherent epitaxial growth of oxide spacers. If a single material cannot simultaneously satisfy all four criteria, composite or engineered spacer architectures may provide an alternative design pathway.

These conclusions provide general guidelines for spacer design based on interfacial reaction pathways and lattice strain in ordered alloy multilayers. The insights obtained here are not limited to the Fe-Pt system but are applicable to a broader class of multilayer alloys involving ordered–ordered phase interfaces.

### **CRedit authorship contribution statement**

Y.K.T. conceptualized this project, designed the experiments and observed microstructure by TEM. The samples were grown and characterized (XRD, Magnetization) by D.O.. MOKE measurements were performed by Y.S. Micromagnetic calculation was done by A.B. Phase-Field (PF) calculation was carried out by Y.M.. S.I., M.O. T.A. and S.K. supported the experiments and PF calculation. D.O., Y.M., Y.S., A.B., and Y.K.T. wrote the first manuscript. All authors analyzed the data, discussed the results, and contributed to the final version of the paper.

### **Declaration of competing interest**

The authors declare that they have no known competing financial interests or personal relationships that could have appeared to influence the work reported in this paper.

### **Supporting information**

Latest phase diagram of Fe-Pt system; peak fitting of (002) in the XRD of Pt-spacer sample; two different Curie temperatures in Pt-spacer sample; elemental mapping of C in the Ag-spacer sample; magnetization behavior of the top and bottom FePt layers.

### **Acknowledgement**

We thank Yukie Mori for preparing the samples for cross-sectional TEM measurements. This work was supported in part by the JST-CREST (JPMJC22C3) and MEXT program: Data Creation

and Utilization-Type Material Research and Development Project (JPMXP1122715503). A part of this work was supported by the Electron Microscopy Unit, National Institute for Materials Science (NIMS). We appreciate the research funding from Seagate Technology. The authors acknowledge JX Advanced Metals Corporation for providing the FePt target used in this work.

## References

1. Suto, H.; Nagasawa, T.; Kudo, K.; Kanao, T.; Mizushima, K.; Sato, R. Layer-Selective Switching of a Double-Layer Perpendicular Magnetic Nanodot Using Microwave Assistance. *Phys. Rev. Applied.* **2016**, *5*, 014003.
2. Tozman, P.; Isogami, S.; Suzuki, I.; Bolyachkin, A.; Sepehri-Amin, H.; Greaves, S.J.; Sasaki, Y.; Chang, T.Y.; Kubota, Y.; Steiner, P.; Huang, P.-W.; Hono, K.; Takahashi, Y.K. Dual-Layer FePt-C Granular Media for Multi-Level Heat-Assisted Magnetic Recording. *Acta Mater.* **2024**, *274*, 119996.
3. Suto, H.; Nagawasa, T.; Kudo, K.; Mizushima, K.; Sato, R. Nanoscale layer-selective readout of magnetization direction from a magnetic multilayer using spin-torque oscillator. *Nanotechnology*, **2014**, *25*, 245501.
4. Kobayashi, T.; Nakatani, Y.; Fujiwara, Y. Media Design for Three-Dimensional Heat-Assisted Magnetic Recording. **2020**, *44*, 122.
5. Chang, T.Y.; Steiner, P.; Venugopal, A.; Jury, J.; Huang, P.W. A. Ghoreyshi, S. Hernandez, Zero-State Insepy Dual-Layer HAMR Media Recording. *IEEE Trans. Magn.* **2022**, *59*, 3200107.
6. Parkin, S.S.P.; Hayashi, M.; Thomas, L. Magnetic domain-wall racetrack memory, *Science*, **2008**, *320*, 190.
7. Yuasa, S.; Nagahama, T.; Fukushima, A.; Suzuki, Y.; Ando, K. Giant room-temperature magnetoresistance in single-crystal Fe/MgO/Fe magnetic tunnel junctions, *Nature Mater.*, **2004**, *3*, 868.
8. Parkin, S.S.P.; Kaiser, C.; Panchula, A.; Rice, P.M.; Hughes, B.; Samant, M.; Yang, S.H. Giant tunnelling magnetoresistance at room temperature with MgO (100) tunnel barriers. *Nature Mater.* **2004**, *3*, 862.
9. Sihombing, R.; Scheike, T.; Uzuhashi, J.; Yasufuku, H.; Ohkubo, T.; Wen, Z.; Mitani, S.; Sukegawa, H. High entropy oxide epitaxial films with interface perpendicular magnetic anisotropy and tunnel magnetoresistance effect toward spintronics applications. *Mater. Today* **2025**, *88*, 12.
10. Takahashi, Y.K.; Srinivasan, A.; Varaprasad, B.; Rajanikanth, A.; Hase, N.; Nakatani, T.M.; Kasai, S.; Furubayashi, T.; Hono, K.; Large magnetoresistance in current-perpendicular-to-

- plane pseudospin valve using a  $\text{Co}_2\text{Fe}(\text{Ge}_{0.5}\text{Ga}_{0.5})$  Heusler alloys. *Appl. Phys. Lett.* **2011**, *98*, 152501.
11. Liu, H-X.; Honda, Y.; Taira, T.; Matsuda, K-I.; Arita, M.; Uemura, T.; Yamamoto, M. Giant tunneling magnetoresistance in epitaxial  $\text{Co}_2\text{MnSi}/\text{MgO}/\text{Co}_2\text{MnSi}$  magnetic tunnel junctions by half-metallicity of  $\text{Co}_2\text{MnSi}$  and coherent tunneling. *Appl. Phys. Lett.* **2012**, *101*, 132418.
  12. Ikeda, S.; Miura, K.; Yamamoto, H.; Mizunuma, K.; D. Gan, H.D.; Endo, M.; Kanai, S.; Hayakawa, J.; Matsukura, F.; Ohno, H. A perpendicular-anisotropy  $\text{CoFeB}/\text{MgO}$  magnetic tunnel junction. *Nature Mater.* **2010**, *9*, 721.
  13. Johnson, M.T.; J.H. Bloemen, P.J.H.; den Broeder, F.J.A.; de Vries, J.J. Magnetic anisotropy in metallic multilayers, *Reports on Progress in Physics*, **1996**, *59*, 1409.
  14. Worledge, D.C.; Hu, G.; Abraham, D.W.; Z. Sun, J.Z.; Trouilloud, P.L.; Nowak, J.; Brown, S.; Gaidis, M.C.; O'Sullivan, E.J.; Robertazzi, R.P. Spin torque switching of perpendicular  $\text{Ta}/\text{CoFeB}/\text{MgO}$ -based magnetic tunnel junctions. *Appl. Phys. Lett.* **2011**, *98*, 022501.
  15. Ohno, H.; Making nonmagnetic semiconductors ferromagnetic, *Science* **1998**, *281*, 951.
  16. Song, T.C.; Cai, X.H.; Tu, M.W.Y.; Zhang, X.O.; Huang, B.V.; Wilson, N.P.; Seyler, K.L.; Zhu, L.; Taniguchi, T.; Watanabe, K.; McGuire, M.A.; Cobden, D.H.; Xiao, D.; Yao, W.; Xu, X.D. *Science* **2018**, *360*, 1214.
  17. Takahashi, Y.K.; Kasai, S.; Furubayashi, T.; Mitani, S.; Inomata, K.; Hono, K. High spin-filter efficiency in a Co ferrite fabricated by a thermal oxidation. *Appl. Phys. Lett.* **2010**, *96*, 072512.
  18. Okamoto, S.; Kikuchi, N.; Kitakami, O.; Miyazaki, T.; Shimada, Y.; Fukamichi, K. Chemical-order-dependent magnetic anisotropy and exchange stiffness constant of  $\text{FePt}$  (001) epitaxial films, *Phys. Rev. B.* **2002**, *66*, 024413.
  19. Suzuki, I.; Kubo, S.; Sepehri-Amin, H.; Takahashi, Y.K. Dependence of the growth mode in epitaxial  $\text{FePt}$  films on surface free energy, *ACS Appl. Mater. Interfaces*, **2021**, *13*, 16620.
  20. Burkert, T.; Eriksson, O.; Simak, S.I.; Ruban, A.V.; Sanyal, B.; Nordstrom, L.; Wills, J.M. Magnetic anisotropy of  $\text{L}_{10}\text{FePt}$  and  $\text{Fe}_{1-x}\text{Mn}_x\text{Pt}$ , *Phys. Rev. B.* **2005**, *71*, 134411.
  21. Ivanov, O.A. Determination of the anisotropy constant and saturation magnetization and magnetic properties of powders of an Iron-Platinum alloy. *Physics of Metals and Metallography.* **1973**, *35*, 81.

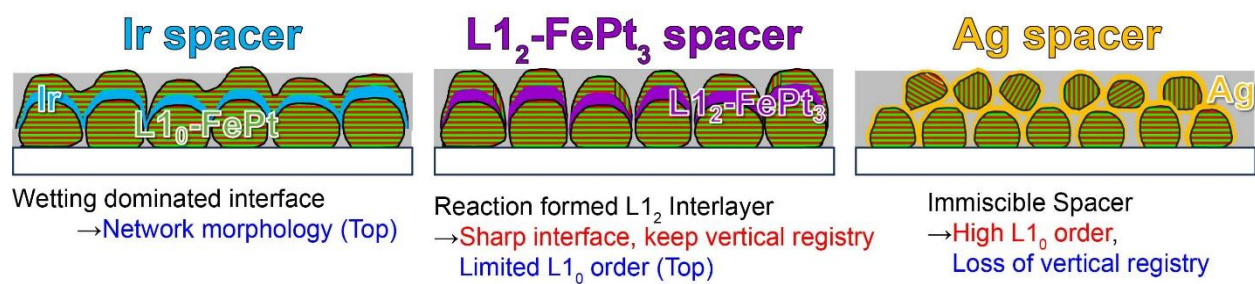
22. Sakuma, A. First principle calculation of the magnetocrystalline anisotropy energy of FePt and CoPt ordered alloys. *J. Phys. Soc. Jpn.* **1994**, *63*, 3053.
23. Farrow, R.F.C.; Weller, D.; Marks, R.F.; Toney, M.F.; Cebollada, A.; Harp, G.R. Control of the axis of chemical ordering and magnetic anisotropy in epitaxial FePt films. *J. Appl. Phys.* **1996**, *76*, 5967.
24. Toney, M.F.; Lee, W-Y.; Hedstrom, J.A.; Kellock, A. Thickness and growth temperature dependence of structure and magnetism in FePt thin films. *J. Appl. Phys.* **2003**, *93*, 9902.
25. Hotta, A.; Ono, T.; Kikuchi, N.; Okamoto, S.; Kitakami, O.; Shimatsu, T. Magnetic anisotropy and crystal domain variant in L1<sub>0</sub>-FePt polycrystalline films. *IEEE Trans. Magn.* **2016**, *52*, 3200803.
26. Sepehri-Amin, H.; Iwama, H.; Ohkubo, T.; Shima, T.; Hono, K. Microstructure and in-plane component of L1<sub>0</sub>-FePt films deposited on MgO and MgAl<sub>2</sub>O<sub>4</sub> substrates. *Scr. Mater.* **2017**, *130*, 247.
27. Moriyama, T.; Mitani, S.; Seki, T.; Shima, T.; Takanashi, K.; Sakuma, A. Magnetic tunnel junctions with L1<sub>0</sub>-ordered FePt alloy electrodes. *J. Appl. Phys.* **2004**, *95*, 6789.
28. Kohn, A.; Tal, N.; Elkayam, A.; Kovacs, A.; Li, D.; Wang, S.; Ghannadzadeh, S.; Hesjedal, T.; Ward, R.C.C. Structure of epitaxial L1<sub>0</sub>-FePt/MgO perpendicular magnetic tunnel junctions. *Appl. Phys. Lett.* **2013**, *102*, 062403.
29. Yang, D.; Li, D.L.; Wang, S.G.; Ma, Q.L.; Liang, S.H.; Wei, H.X.; Han, X.F.; Hesjedal, T.; Ward, R.C.C.; Kohn, A.; Elkayam, A.; Tal, N.; Zhang, X.-G. Effect of interfacial structures on spin dependent tunneling in epitaxial L1<sub>0</sub>-FePt/MgO/FePt perpendicular magnetic tunnel junctions. *J. Appl. Phys.* **2015**, *117*, 083904.
30. Ogawa, D.; Bolyachkin, A.; Dilipan, A.R.; Kulesh, N.; Sepehri-Amin, H.; Takahashi, Y.K. Exchange-coupled Fe-Pt/Ru/Fe-Pt nanogranular films as potential heat-assisted-magnetic-recording media with reduced writing temperature. *Phys. Rev. Applied.* **2024**, *22*, 054060.
31. Verna, A.; Alippi, P.; Offi, F.; Barucca, G.; Varvaro, G.; Agostinelli, E.; Albrecht, M.; Rutkowaki, B.; Ruocco, A.; Paoloni, D.; Valvideare, M.; Laureti, S. Disclosing the nature of asymmetric interface magnetism in Co/Pt multilayers. *ACS Appl. Mater. Interfaces.* **2022**, *14*, 10.
32. Kuz'min, M.D. Shape of Temperature Dependence of Spontaneous Magnetization of Ferromagnets: Quantitative Analysis. *Phys. Rev. Lett.* **2005**, *94*, 107204.

33. Steinbach, I. Phase-field models in materials science. *Model. Simul. Mater. Sci. Eng.* **2009**, *17*, 1–31.
34. Hilliard, J.E. Phase Transformation (ed. H.I. Aaronson), 497. ASM, Metals-Park, Ohio (1970).
35. Tanaka, M.; Muramatsu, M. ; Ode, M.; Abe, T. Thermodynamic reassessment of the Fe-Pt system. *Calphad* **2025**, *90*, 102868.
36. Dannenberg, A.; Gruner, M.E.; Hucht, A.; Entel, P. Surface Energies of Stoichiometric FePt and CoPt Alloys and Their Implications for Nanoparticle Morphologies. *Phys. Rev. B* **2009**, *80* 245438.
37. Tyson, W.R.; Miller, W.A. Surface Free Energies of Solid Metals: Estimation from Liquid Surface Tension Measurements. *Surf. Sci.* **1977**, *62*, 267.
38. Vitos, L.; Ruban, A.V.; Skriver, H. L.; Kollár, J. Surface Properties of Metals from First Principles. *Surf. Sci.* **1998**, *411* 186.
39. Shima, T.; Takanashi, K.; Takahashi, Y.K.; Hono, K. *Appl. Phys. Lett.* **2002**, *81*, 1050.
40. Takahashi, Y.K.; Hono, K.; Shima, T.; Takanashi, K. Microstructure and magnetic properties of FePt thin films epitaxially grown on MgO(001) substrates. *J. Magn. Magn. Mater.* **2003**, *267*, 248.
41. Nozaki, T.; Koziol-Rachwal, A.; Tsujikawa, M.; Shiota, Y.; Xu, X.; Ohkubo, T.; Tsukahara, T.; Miwa, S.; Suzuki, M.; Tamaru, S.; Kubota, H.; Fukushima, A.; Hono, K.; Shirai, M.; Suzuki, Y.; Yuasa, S. Highly Efficient Voltage Control of Spin and Enhanced Interfacial Perpendicular Magnetic Anisotropy in Iridium-Doped Fe/MgO Magnetic Tunnel Junctions. *NPG Asia Mater.* **2017**, *9*, e451.
42. Maat, S.; Hellwig, O.; Zelzer, G.; Fullerton, E.E.; Mankey, G.J.; Crow, M.L.; Robertson, J.L. Antiferromagnetic structure of FePt<sub>3</sub> films studied by neutron scattering, *Phys. Rev. B.* **2001**, *63*, 134426.
43. Varaprasad, B. S. D. Ch. S.; Takahashi, Y.K.; Wang, J.; Ina, T.; Nakamura, T.; Ueno, W.; Nitta, K.; Uruga, T.; Hono, K. Mechanism of coercivity enhancement by Ag addition in FePt-C granular films for heat assisted magnetic recording media. *Appl. Phys. Lett.*, **2014**, *104*, 222403.
44. Suzuki, I.; Sepehri-Amin. H.; Hono, K.; Takahashi, Y.K. Control of grain density by varying lattice mismatch in FePt-C film for heat assisted magnetic recording, *J. Alloys Compd.* **2023**, *968*, 172196.

45. Cahn, J.W. ; Hilliard, J.E. Free Energy of a Nonuniform System. I. Interfacial Free Energy. *J. Chem. Phys.* **1958**, 28, 258.
46. Srinivasan, R.; Banerjee, R.; Hwang, J.Y.; Viswanathan, G.B.; Tiley, J.; Dimiduk, D.M.; Fraser, H.L.. Influence of Elastic Strains on Spinodal Decomposition Kinetics in Metallic Systems. *Phys. Rev. Lett.* **2009**, 102, 196101.
47. Ardell, A.J. The Effect of Interface Curvature on Coarsening During Precipitation in Multicomponent Systems. *Scr. Mater.* **2012**, 66, 423.
48. Forghani, F.; Han, J.C.; Moon, J.; Abbaschian, R.; Park, C.G.; Kim, H.S.; Nili-Ahmadabadi, M. Grain Boundary Character Distribution and Its Effect on Mechanical Properties in Ultrafine-Grained Materials. *J. Alloys Compd.* **2019**, 777, 1222–1229.
49. Asta, M.; Hoyt, J.J. Thermodynamic Properties of Solid–Liquid Interfaces in Alloys from Atomistic Simulations. *Acta Mater.* **2000**, 48, 1089–1095.
50. Lass, E.A.; Johnson, W.C.; Shiflet, G.J. The Influence of Interface Mobility Anisotropy on Precipitate Morphology in Ni–Al Alloys. *Calphad* **2006**, 30 42–50.
51. Hoyt, J.J. Molecular Dynamics Study of the Influence of Anisotropy on Solid–Liquid Interface Migration. *Phys. Rev. B* **2007**, 76, 094102.



## Graphical abstract



Figures.

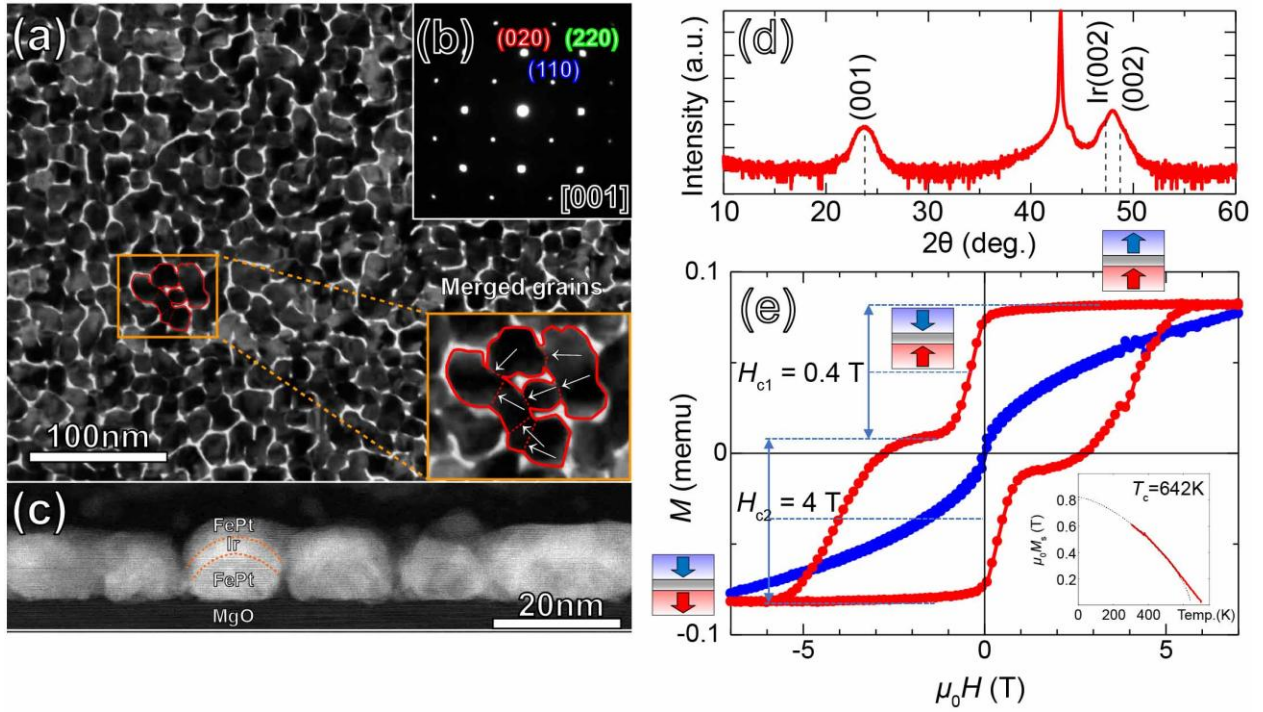


Figure 1 Interfacial wetting-driven microstructure and magnetic response of FePt-20vol.%C(4.5 nm)/Ir-20vol.%C(2.9 nm)/FePt-20vol.%C(4.5nm) film. (a) in-plane BF-TEM image, (b) SAED pattern, (c) cross-sectional HAADF-STEM image, (d) XRD pattern, (e) out-of-plane (red line) and in-plane (blue line) magnetization curves. Inset of (e) is the temperature dependence of magnetization. These results indicate that Ir spacers preserve  $L1_0$  ordering but induce a wetting-dominated network morphology, which modifies the magnetization reversal behavior without fundamentally degrading magnetic anisotropy.

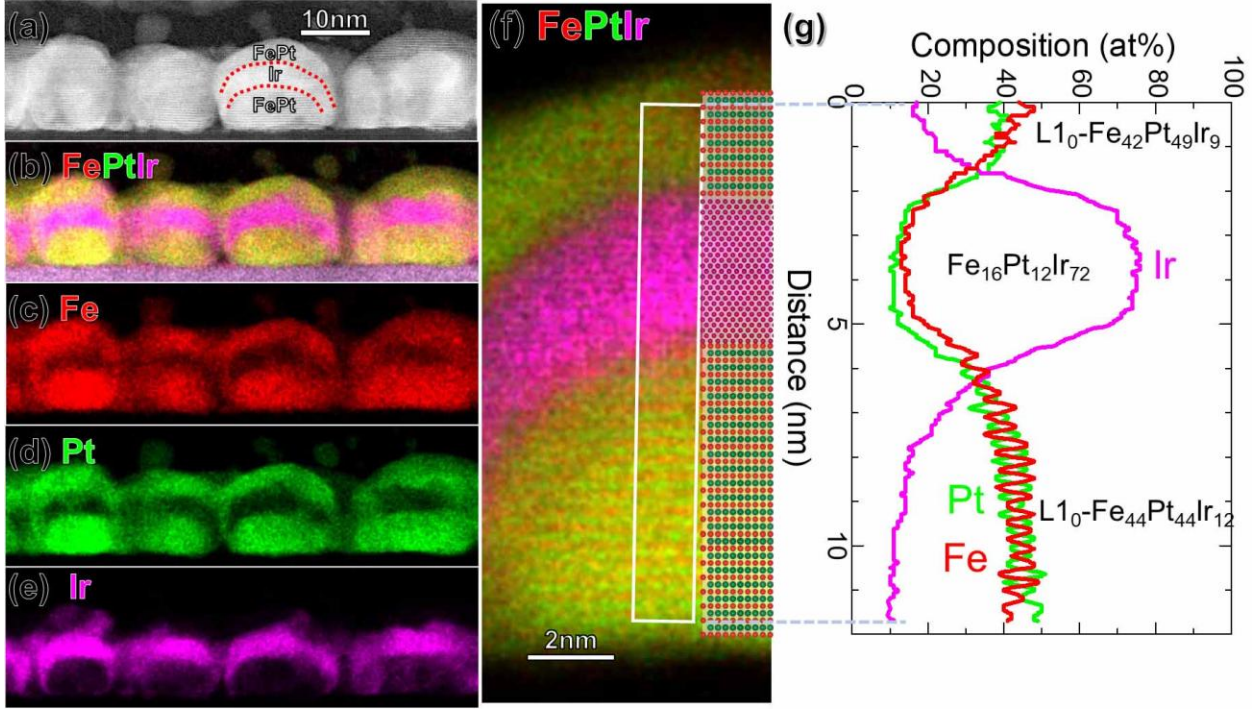


Figure 2 (a) HAADF-STEM image and (b)~(f) corresponding elemental maps of FePt-20vol.%C(4.5 nm)/Ir-20vol.%C(2.9 nm)/FePt-20vol.%C(4.5nm) film. (g) compositional line profile of the rectangular region of (f).

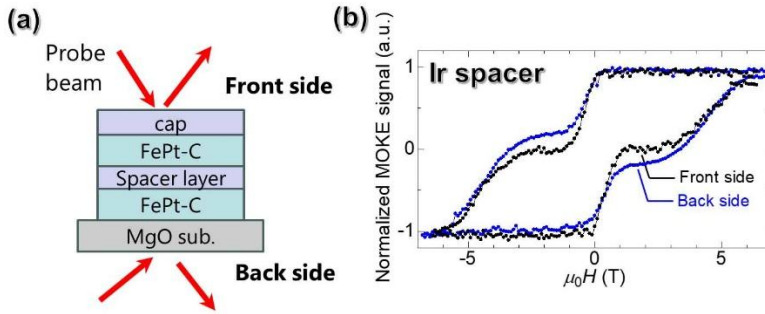


Figure 3 (a) schematic view of the film and probe beam direction. MOKE hysteresis loops with Ir spacer. Black and blue lines correspond to the MOKE hysteresis irradiated the probe beam from the back and the front sides, respectively. These hysteresis loops demonstrate layer-specific magnetization behavior, confirming decoupling of magnetization in top and bottom FePt layers.



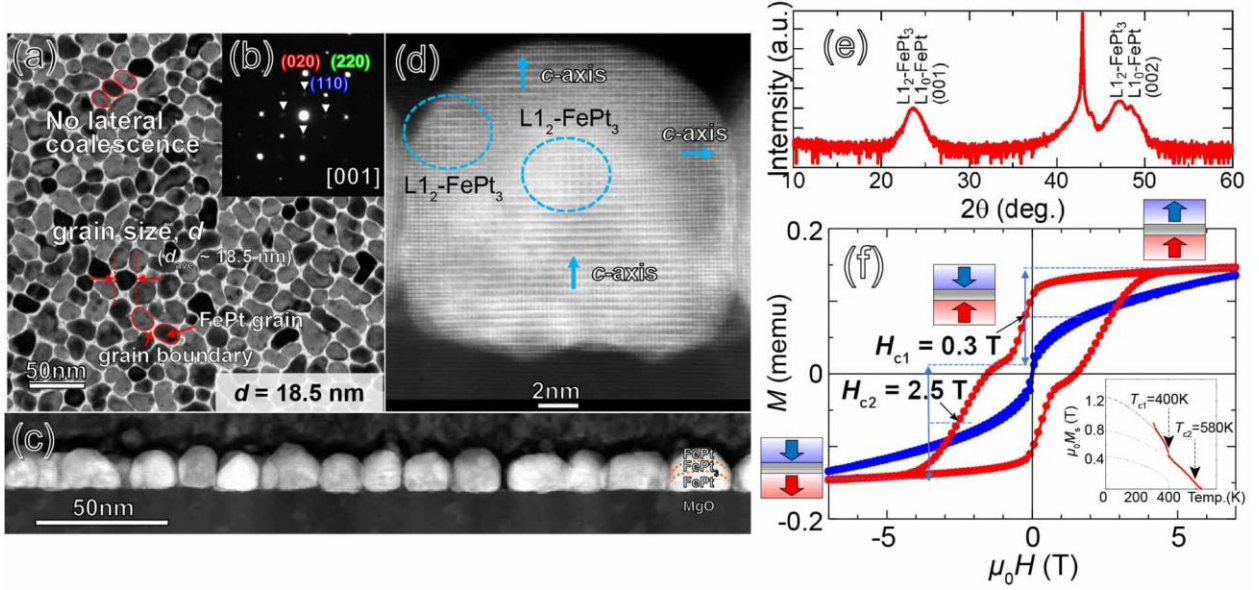


Figure 4 Interfacial reaction-induced ordering limitation in FePt-20vol.%C(4.5 nm)/Pt-20vol.%C(2.9 nm)/FePt-20vol.%C(4.5nm) film. (a) in-plane BF-TEM image, (b) SAED pattern, (c)(d) cross-sectional HAADF-STEM images, (e) XRD pattern, (f) out-of-plane (red line) and in-plane (blue line) magnetization curves. Arrows in (d) indicate direction of  $c$ -axis of FePt. Inset in (f) is the temperature dependence of the magnetization. The reduced coercivity of the top FePt layer reflects the limited  $L_{10}$  ordering caused by small lattice strain in the interface as revealed by the microstructural analyses.

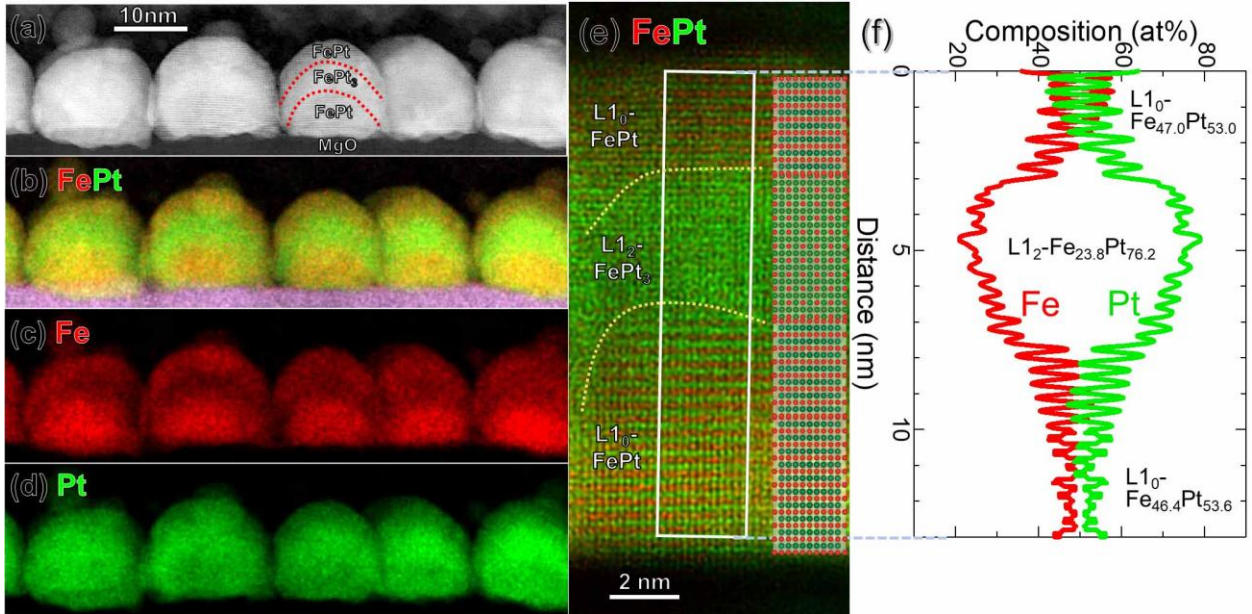


Figure 5 (a) cross-sectional HAADF-STEM image and (b)~(e) corresponding elemental maps of FePt-20vol.%C(4.5 nm)/Pt-20vol.%C(2.9 nm)/FePt-20vol.%C(4.5nm) film. (f) compositional line profile of the rectangular region of (e). These compositional profiles demonstrate that the

interfacial layer deviates from the stoichiometry required for highly ordered L1<sub>0</sub>-FePt, providing a structural origin for the degraded magnetic hardness of the overgrown layer.

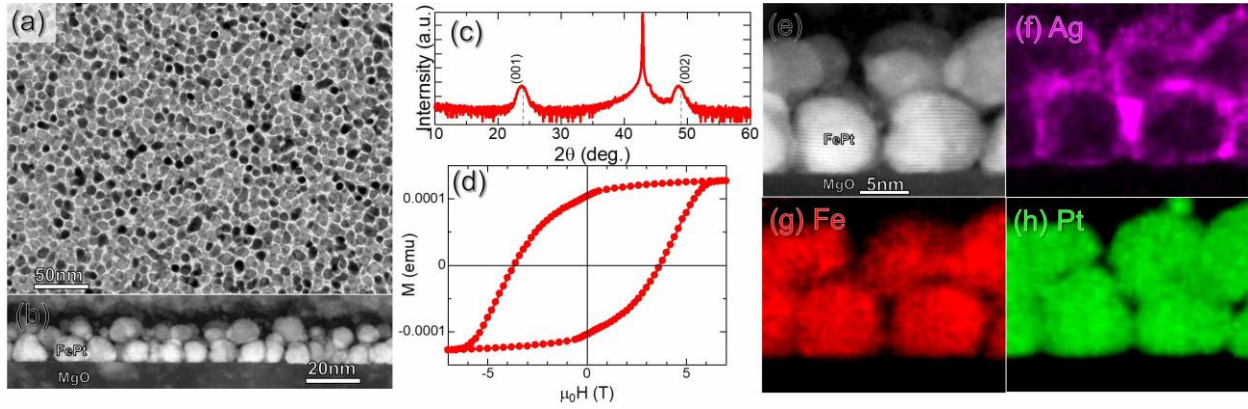


Figure 6 Immiscibility-driven loss of epitaxial registry in FePt-20vol.%C(4.5 nm)/Ag-20vol.%C(2.9 nm)/FePt-20vol.%C(4.5nm) film and its magnetic consequence. (a) in-plane BF-TEM image and (b) cross-sectional STEM-HAADF image, (c) XRD pattern, (d) out-of-plane magnetization curve, (e)~(h) elemental maps. Although Ag spacers yield high L1<sub>0</sub> ordering ( $S = 0.75$ ) and a single-step reversal with  $\mu_0 H_c = 3.5$  T, the HAADF-STEM image demonstrates the loss of vertical registry between bottom and top FePt grains, indicating a trade-off between chemical immiscibility and epitaxial continuity.

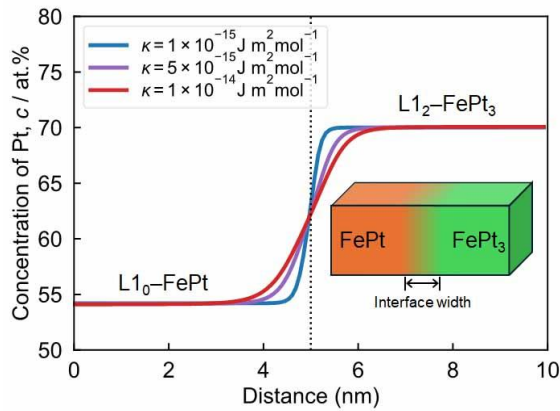


Figure 7 The Pt concentration profiles across the L1<sub>0</sub>-FePt-L1<sub>2</sub>-FePt<sub>3</sub> interface calculated by phase-field (PF) simulation. The dashed line indicates the center of the interface.